Journal of Materials Chemistry A

RSC Publishing

PAPER

View Article Online
View Journal | View Issue

Cite this: J. Mater. Chem. A, 2013, 1, 13510

Reversible hydrogen sorption in $NaBH_4$ at lower temperatures

Lina Chong,[a] Jianxin Zou,*[ab] Xiaoqin Zeng[ab] and Wenjiang Ding[ab]

Received 18th June 2013
Accepted 4th September 2013

DOI: 10.1039/c3ta12369c

www.rsc.org/MaterialsA

In the present study, a new hydrogen storage system, being able to reversibly absorb/desorb hydrogen at fairly low temperatures, was developed based on a $3NaBH_4$–PrF_3 composite. It is shown that 3 wt% of reversible hydrogen sorption can be achieved in the $3NaBH_4$–PrF_3 composite at 400 °C with fast kinetics. After the addition of 5 mol% VF_3, the dehydrogenation kinetics of the $3NaBH_4$–PrF_3 composite can be significantly improved. The onset dehydriding temperature is lowered down to 46 °C in vacuum, and the dehydrogenation finishes in 2 min at 400 °C. Both the dehydrogenation enthalpy and activation energy of $3NaBH_4$–PrF_3 can be lowered down through the addition of VF_3. In particular, the dehydrogenation products of the $3NaBH_4$–PrF_3–5 mol% VF_3 composite can be rehydrogenated at a temperature as low as 48 °C with the regeneration of $NaBH_4$. At 84 °C, a reversible hydrogen sorption of about 1.2 wt% can be achieved in the $3NaBH_4$–PrF_3–5 mol% VF_3 composite. The improvement in hydrogen sorption properties can be mainly attributed to the formation of the VB_2 phase during dehydrogenation as an efficient catalyst, which maintains well its catalytic effect in the re-/dehydrogenation cycles. Based on a series of controlled experiments and phase analyses, the de-/rehydrogenation mechanisms of the $3NaBH_4$–PrF_3 composite without and with VF_3 addition are proposed and discussed in detail.

1. Introduction

Hydrogen energy has long been considered as the most promising energy source for future human society due to its advantages, such as cleanness, inexhaustible resources, high efficiency and environmental friendliness. However, hydrogen storage is now becoming the bottleneck towards the future "hydrogen economy". Among different hydrogen carriers, solid-state hydrogen storage materials hold remarkable potential for on-board and stationary applications. In particular, metal hydrides have been widely accepted as highly desirable hydrogen carriers due to their high safety and high gravimetric/volumetric hydrogen content.[1–3] Recently, metal borohydrides $M(BH_4)_n$ have been extensively investigated as potential on-board hydrogen storage carriers owing to their high gravimetric hydrogen contents and good stability at room temperature.[4–7] However, the unfavorable thermodynamic and kinetic properties of this class of materials have limited their practical applications.[8,9] Much research has focused on improving the hydrogen storage properties of the widely known borohydrides such as $LiBH_4$, $NaBH_4$, $Ca(BH_4)_2$ and $Mg(BH_4)_2$.[1–3] Different systems containing these borohydrides and catalysts/reagents have been developed in the past decade. However, none could meet the targets set by the U. S. Department of Energy (DOE) for on-board hydrogen carriers.[10] The high operating temperature and poor reversibility are the major problems faced by borohydride containing hydrogen storage materials.

$NaBH_4$, the first known borohydride, is fairly stable in air and has gravimetric and volumetric hydrogen contents of 10.8 wt% and 115 kg of H_2 m^{-3}, respectively. Most studies on $NaBH_4$ focused on catalyzed hydrolysis which was so far one of the possible approaches to utilize its high hydrogen capacity for onboard applications.[11] Alternatively, $NaBH_4$ can yield hydrogen through thermal decomposition by the following reaction:

$$NaBH_4 \rightarrow Na + B + 2H_2. \quad (1)$$

However, the standard formation enthalpy of $NaBH_4$ is -191.836 kJ mol^{-1},[12] which means that $NaBH_4$ is thermodynamically very stable. Consequently, its decomposition starts at about 565 °C,[6,13,14] which is apparently too high to be used as an on-board hydrogen carrier.

Many approaches, such as reactant destabilization,[15–18] nanoconfinement[19] in nanoporous scaffolds and catalyst addition,[20] have been employed to ameliorate the thermodynamics and kinetics of $NaBH_4$. One promising approach is to add metal hydrides into $NaBH_4$ to form $yNaBH_4/MH_x$ type composites. In these composites, corresponding metal-borides would be

[a]Shanghai Engineering Research Center of Magnesium Materials and Application, National Engineering Research Center of Light Alloy Net Forming, Shanghai Jiao Tong University, Shanghai 200240, China. E-mail: zoujx@sjtu.edu.cn; Fax: +86-21-34203730; Tel: +86-21-54742381

[b]State Key Laboratory of Metal Matrix composite, School of Materials Science and Engineering, Shanghai Jiao Tong University, Shanghai 200240, China

formed after dehydrogenation. The formation of metal-borides, such as MgB_2, CaB_6, *etc.*, not only stabilizes the dehydrogenated products, but also allows the rehydrogenation to take place under moderate conditions due to the fact that the activation energy needed to break the B–M bond is remarkably lower than that needed for the B–B bond.[21] Thus, it is essential to employ a material which will react with $NaBH_4$ to produce metal-borides during dehydrogenation. Reducing the enthalpy gap between desorption products and $NaBH_4$ as mentioned above is important for making $NaBH_4$ reversible under moderate conditions for practical applications. It has been established recently that metal fluorides have similar effects as metal hydrides. Indeed, F^- and H^- have quite similar ionic radii and chemical properties. The rare-earth borides constitute a class of materials which possess interesting and unique physical and chemical properties, such as superconductivity and ferromagnetism.[22–24] The boron atoms may form two-dimensional networks and three-dimensional frameworks in rare-earth borides.[25] Moreover, the standard enthalpies of formation of some lanthanide borides are lower than other metal-borides when they are formed in borohydride containing hydrogen storage systems. For instance, standard formation enthalpies of PrB_4 and PrB_6 are -265.5 ± 8 and -359.1 ± 39.9 kJ mol^{-1},[25] respectively, which are much lower than those of MgB_2 (-93.221 kJ mol^{-1} (ref. 26)) and CaB_6 (-123.591 kJ mol^{-1} (ref. 27)). Therefore, it is easier to form B–Pr phases than to form MgB_2 or CaB_6. Recently, rare earth containing additives have been investigated to destabilize borohydrides in different hydrogen storage systems, such as RCl_3 (R = Y, Dy, Gd),[28] and CeH_2[29] in $LiBH_4$ based systems and NdF_3[30] and YF_3[31] in $NaBH_4$ based systems. In our recent study on the $3NaBH_4$–NdF_3 system, we have demonstrated that NdF_3 could significantly improve the hydrogen storage performance of $NaBH_4$ by the formation of NdB_6 during the dehydrogenation process, which is the key factor for reversibility. Theoretical calculations indicated that F^- anions may participate in the dehydrogenation reaction by lattice substitution for the H^- anions,[32] which could result in favorable thermodynamic modifications. Such an effect was named as "functionality" of F^- anions. It was demonstrated that the addition of transition metal (TM) compounds to borohydrides as catalysts could significantly enhance the hydrogen de/absorption kinetics of borohydrides owing to the catalytic role of the transition metals or their cations. Bosenberg *et al.*[33] reported that V-based additives significantly enhanced the reaction kinetics in hydride containing composites. Moreover, Zaluska and Zaluski[34] claimed that anions (N^{3-}, O^{2-}, *etc.*) could be incorporated into a catalyst complex to play a critical role in tuning the activity of the catalyst for hydrogen dissociation/recombination. On the other hand, Barkhordarian[35] *et al.* proposed that F^- anions could provide electron-rich centers to trap transition metal cations, and thereby tailor the electronic structure of the transition metal cations to influence its activity for hydrogen dissociation/recombination.

Motivated by the above theoretical and experimental findings, we further extended our study to investigate the effect of lanthanide fluoride–PrF_3– on hydrogen sorption in $NaBH_4$, as well as the effect of the addition of VF_3 as a catalyst on the binary system-$3NaBH_4$–PrF_3. Our study reveals that the addition of PrF_3 into $NaBH_4$ could result in a notable decrease of the dehydrogenation temperature and an increase in hydrogen sorption kinetics of $NaBH_4$. In addition, the minor addition of VF_3 as a catalyst leads to further improvement in dehydrogenation kinetics and allows the rehydrogenation of $NaBH_4$ to occur at lower temperatures (*i.e.* 48 °C). Based on the experimental investigations, the mechanisms of de-/rehydrogenation in binary $3NaBH_4$–PrF_3 and ternary $3NaBH_4$–PrF_3–5 mol% VF_3 composites are proposed and discussed in detail. The results gathered in this study will show the potential to achieve reversible hydrogen sorption in $NaBH_4$ at lower temperatures through the co-addition of 4f rear earth fluorides as reagents and 3d transition metal fluorides as catalysts.

2. Experimental

Commercially available $NaBH_4$ (~95%) was purchased from Aladdin Reagent Database, Inc. PrF_3 (99.9%) and VF_3 (98%) powders were obtained from Alfa Aesar. All of the chemicals were used as received without further purification. The sample storage and handling were performed in a Lab 2000 glove box (Etelux Intertgas system Co., Ltd.) filled with purified argon. The $3NaBH_4$–PrF_3 mixture was prepared by mechanical ball milling under an Ar atmosphere for 16 h using a QM-1SP2 planetary ball mill at 456 rpm in a stainless steel vessel. For the ternary composite, two grams of $NaBH_4$, PrF_3 and VF_3 in a 3 : 1 : 0.2 molar ratio were milled under the same conditions for the sake of comparison. The stainless steel vessel for ball milling was 100 ml, and the weight ratio of the sample to the ball was 1 : 30.

Hydriding/dehydriding properties of the samples were measured by using a Sievert type apparatus manufactured by the Shanghai Institute of Microsystem and Information Technology. The pressure-concentration-temperature (PCT) measurements were performed at different temperatures in the hydrogen pressure range of 0.001–4.6 MPa. Before each dehydrogenation kinetic measurement, the sample chamber was first filled with 5 MPa hydrogen, then after the temperature was quickly raised to and kept at the desired ones, the sample chamber was quickly evacuated. All the samples were thoroughly dehydrogenated at 415 °C for 2 h under dynamic vacuum before each rehydrogenation kinetic measurement. For the ternary system, some samples were rehydrogenated at relatively low temperatures (*i.e.* 48 °C, 84 °C, 102 °C and 150 °C) under an initial hydrogen pressure of 3.2 MPa. The subsequent hydrogen desorption measurements were carried out at 84 °C and 100 °C under an initial hydrogen pressure of 0 and 0.9 MPa. Temperature-programmed-dehydrogenation (TPD) measurements were performed for both the binary and ternary composite samples starting from vacuum at a heating rate of 3 °C min^{-1}. The absorbed/desorbed hydrogen was determined by volumetric methods. For comparison, the weights of VF_3 were taken into account in the determination of the H-capacity of the ternary composite.

Dehydriding behaviors of samples were examined by synchronous thermal analyses using a thermogravimeter/differential scanning calorimeter (TG/DSC, Netzsch, STA 449 F3

Jupiter) equipped with a mass spectrometer (MS, HIDEN, HPR-20 QIC, Gas Analysis System). The heating rate was set at 3, 5 and 10 K min^{-1}, with the temperature rising from 26 to 500 °C under a 1 bar flowing argon atmosphere.

The samples at different states were characterized by X-ray diffraction (XRD Rigaku D/MAX-2500, VL/PCX, Cu Kα radiation), X-ray photoelectron spectroscopy (XPS, A AXIS ULTRADLD, Al Kα radiation), Fourier transform infrared spectrometry (FTIR Spectrum 100 facility, Perkin Elmer, Inc., USA), and Scanning Electron Microscopy (SEM, Hitachi S-4800), as well as Energy Dispersive X-ray Spectroscopy (EDS) attached to SEM. In order to minimize the H_2O/O_2 contamination during the XRD measurements, samples were flattened into the specimen holders covered by arch glass on each side in the Ar filled glove box and sealed with airtight amorphous tape which shows a broad peak around $2\theta = 15°$ in XRD patterns. For the XPS measurements, binding energy calibration of all samples was done using the C 1s peak (284.5 eV), and an Ar + ion gun was used for etching. Vibration spectra of the species in absorbance mode were obtained using a KBr tablet method with the mass ratio of the sample to KBr being 1 : 60 in FITR measurements.

3. Results and discussion

3.1 Thermal de-/rehydrogenation behaviors of the $3NaBH_4$–PrF_3 and $3NaBH_4$–PrF_3–5 mol% VF_3 composites

The dehydrogenation behaviors of the ball-milled $3NaBH_4$–PrF_3 composite without and with VF_3 addition were first evaluated by TG-DSC-MS measurements under a 1 bar argon atmosphere with the heating rate being 10 K min^{-1}. For dehydrogenation of the $3NaBH_4$–PrF_3 composite, Fig. 1(a) shows an endothermic peak together with a mass loss at 439 °C when the heating rate is 10 K min^{-1}, which is about 78 °C lower than that of pure $NaBH_4$ under the same condition.[31] The hydrogen released from the $3NaBH_4$–PrF_3 composite can reach 3.46 wt%, which is fairly close to the theoretical hydrogen content of the composite (3.53 wt%). Fig. 1(b) shows that only H_2 (with a mass of 2) is detected during the dehydrogenation of the $3NaBH_4$–PrF_3 composite. For the thermal decomposition of $3NaBH_4$–PrF_3–5 mol% VF_3, as seen in Fig. 1(a), the endothermic peak is located at 417 °C when the heating rate is 10 K min^{-1}, showing that VF_3 can further lower down the decomposition temperature of $3NaBH_4$–PrF_3. In addition, the TG curve shows that the mass loss starts from 70 °C, and the total mass loss is 3.53 wt%, which is fairly close to the theoretical hydrogen content of the $3NaBH_4$–PrF_3–5 mol% VF_3 composite (3.60 wt%). That is to say, the decomposition of this composite is nearly complete.

To further investigate the desorption behaviors of $3NaBH_4$–PrF_3 without and with 5 mol% VF_3 doping, as well as the effects of VF_3 on the dehydrogenation kinetics, the activation energies of dehydrogenation for the two samples were determined from DSC data using the Kissinger equation:[36]

$$\frac{d\left(\ln\frac{\beta}{T_p^2}\right)}{d\left(\frac{1}{T_p}\right)} = -\frac{E_a}{R}, \quad (2)$$

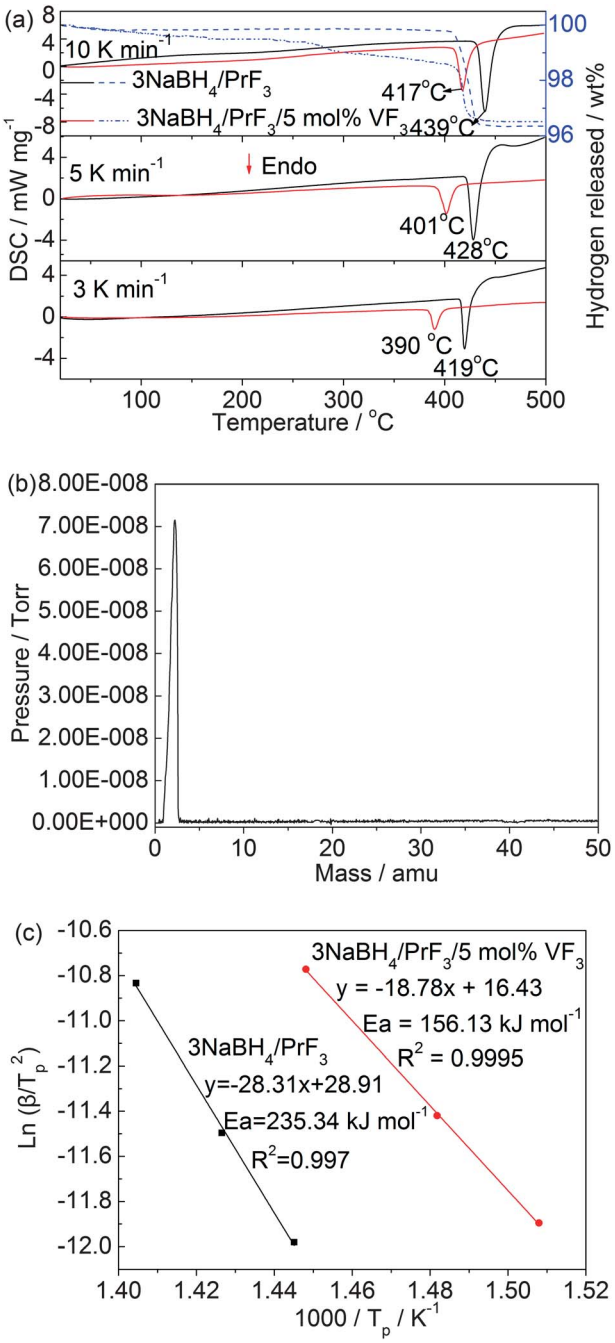

Fig. 1 (a) DSC/TG curves (with the heating rate being 10 K min^{-1}) and DSC curves (with the heating rate being 5 and 3 K min^{-1}) of the $3NaBH_4$–PrF_3 and 5 mol% VF_3-doped $3NaBH_4$–PrF_3 composites under a 1 atm argon atmosphere; (b) MS curve of the $3NaBH_4$–PrF_3 composite in the range of m/z from 0 to 50; (c) Kissinger plots of the dehydrogenation of $3NaBH_4$–PrF_3 and $3NaBH_4$–PrF_3–5 mol% VF_3 composites.

where T_p is the peak temperature corresponding to the heating rate β, E_a the activation energy and R the gas constant. DSC curves for the $3NaBH_4$–PrF_3 and the $3NaBH_4$–PrF_3–5 mol% VF_3 composites with heating rates being 3 and 5 K min^{-1} are also shown in Fig. 1(a). As expected, the endothermic peak corresponding to the maximum rate of dehydrogenation shifted to higher temperatures as the heating rate increased. Table 1

Table 1 The peak desorption temperatures corresponding to the two composites measured by DSC at different heating rates under a 1 bar argon pressure

Sample	Heating rates/K min^{-1}	Peak temperature/°C
$3NaBH_4$–PrF_3	3	419
	5	428
	10	439
$3NaBH_4$–PrF_3–5 mol% VF_3	3	390
	5	401
	10	417

presents the temperatures corresponding to each peak at different heating rates from the DSC curves in Fig. 1(a). The plots based on the Kissinger equation are drawn in Fig. 1(c). It can be seen that the favorable intrinsic linearity of all the curves is well presented by the Kissinger equation. From the obtained results, the activation energy (E_a) for the $3NaBH_4$–PrF_3 composite was 235.3 kJ mol^{-1}, while E_a decreased to 156.1 kJ mol^{-1} when 5 mol% VF_3 was added to the $3NaBH_4$–PrF_3 composite. This result clearly showed that the addition of 5 mol% VF_3 could reduce the dehydrogenation energy barriers for the $3NaBH_4$–PrF_3 composite.

To characterize the de-/rehydrogenation behaviors and investigate their thermodynamic properties, PCT absorption and desorption isothermal curves for the $3NaBH_4$–PrF_3 composite at 380 °C, 400 °C, 415 °C and for the $3NaBH_4$–PrF_3–5 mol% VF_3 composite at 325 °C, 390 °C, 400 °C, 410 °C were collected, as shown in Fig. 2(a). It can be seen that the $3NaBH_4$–PrF_3 composite exhibits stable and long absorption–desorption plateaus, *e.g.*, at 415 °C, the stable absorption plateau starts from about 0.2 to 2.6 wt% and the stable desorption plateau starts from about 2.6 to 0.15 wt%, indicating that the $3NaBH_4$–PrF_3 composite has a good hydrogen storage reversibility. In addition, the reversible hydrogen absorption capacity increases with the increasing temperature, and the dehydrogenation is nearly complete at each testing temperature, as shown in Fig. 2(a)-up. For example, at 380 °C, 400 °C and 415 °C, the reversible hydrogen absorption capacity of the $3NaBH_4$–PrF_3 composite is 2.61, 2.71 and 2.90 wt%, which corresponds to 73.9%, 76.9% and 82.1% of its theoretical value (3.53 wt%), respectively. Furthermore, there is a hysteresis between absorption and desorption isotherms. A similar phenomenon has been observed in the $3NaBH_4$–NdF_3 and $3NaBH_4$–YF_3 systems.[30,31] Fig. 2(a)-down shows the PC isotherms of the $3NaBH_4$–PrF_3–5 mol% VF_3 composite. It reveals the following aspects. Firstly, the $3NaBH_4$–PrF_3–5 mol% VF_3 composite is also a reversible hydrogen storage system with a reversible hydrogen capacity of 2.95 wt% which is 82.0% of its theoretical value (3.60 wt%) at 400 °C. Secondly, no distinct absorption plateaus can be observed in those curves, which is different from the absorption behaviors of the $3NaBH_4$–PrF_3 composite. This means that the hydrogenation equilibrium is not achievable under present conditions. Thirdly, there still exists the phenomenon of hysteresis between absorption and desorption curves. However, the hysteresis was postponed, indicating a better desorption

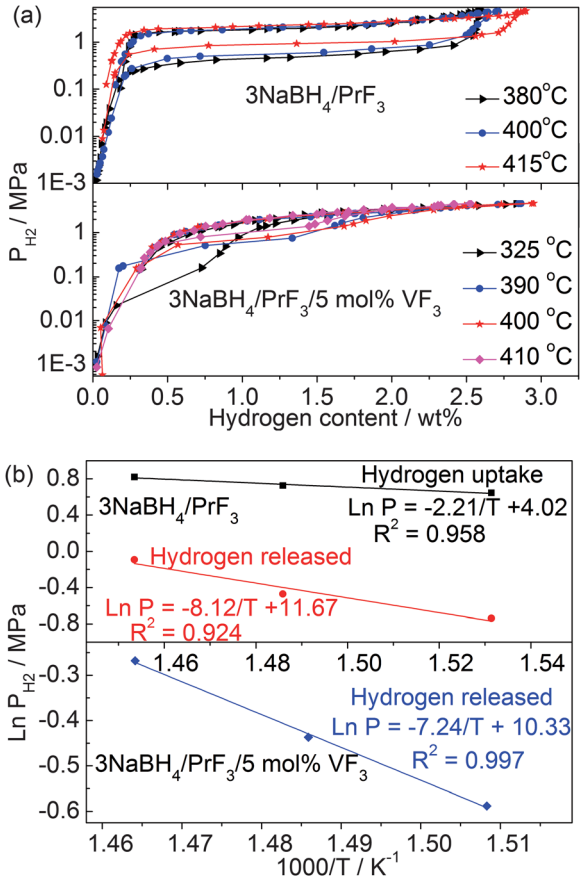

Fig. 2 (a) PCT curves of the $3NaBH_4$–PrF_3 composites measured at 380, 400 and 415 °C, as well as 5 mol% VF_3-doped $3NaBH_4$–PrF_3 composites measured at 325, 390, 400 and 410 °C. (b) van't Hoff diagrams showing de-/rehydrogenation equilibrium pressures over temperatures for the $3NaBH_4$–PrF_3 composites as well as dehydrogenation equilibrium pressure over temperatures for $3NaBH_4$–PrF_3–5 mol% VF_3 composites.

kinetics than that of the $3NaBH_4$–PrF_3 composite. From the comparison of hydrogen sorption behaviors shown in Fig. 2(a), it seems that the addition of VF_3 to $3NaBH_4$–PrF_3 favors the desorption rate but lowers down the absorption rate. The fact that the catalysts have more positive effects in enhancing the dehydrogenation kinetics than hydrogenation kinetics has also been reported in $LiBH_4$ containing systems.[37,38]

Since PrF_3 and VF_3 have positive effects in enhancing the re-/dehydrogenation performance of $NaBH_4$, the thermodynamic parameters, enthalpy and entropy changes, of the $3NaBH_4$–PrF_3 as well as the 5 mol% VF_3-doped $3NaBH_4$–PrF_3 composite during re-/dehydrogenation were calculated by using van't Hoff equation: $\ln(P_{eq}) = -\Delta H/RT + \Delta S/R$, where P_{eq} is the reaction pressure, T is the absolute temperature, and R is the gas constant. Table 2 summarizes the data corresponding to Fig. 2(a). Fig. 2(b) shows the van't Hoff plots for the $3NaBH_4$–PrF_3 composite both for absorption and desorption, and for desorption in the 5 mol% VF_3-doped $3NaBH_4$–PrF_3 composite. For the $3NaBH_4$–PrF_3 composite, van't Hoff equations are expressed as $\ln(P_{eq}/MPa) = -8.12/T + 11.67$ for desorption and $\ln(P_{eq}/MPa) = -2.21/T + 4.02$ for absorption. For the 5 mol% VF_3-doped $3NaBH_4$–PrF_3 composite, van't Hoff equation is

Table 2 PCT data corresponding to Fig. 2(a)

$3NaBH_4$–PrF_3			$3NaBH_4$–PrF_3–5 mol% VF_3			
Temperature/°C	Absorption plateaus/MPa	Desorption plateaus/MPa	Reversible hydrogen sorption/wt%	Temperature/°C	Desorption plateaus /MPa	Reversible hydrogen sorption/wt%
380	1.923	0.509	2.61	390	0.555	2.87
400	2.063	0.631	2.71	400	0.646	2.95
415	2.299	0.954	2.90	410	0.764	2.53

determined to be $\ln(P_{eq}/MPa) = -7.24/T + 10.33$ for dehydrogenation. The dehydrogenation enthalpy of the $3NaBH_4$–PrF_3 and the 5 mol% VF_3-doped $3NaBH_4$–PrF_3 composites is 67.5 kJ mol^{-1} H_2 and 60.2 kJ mol^{-1} H_2, respectively. These values are much smaller than that of $NaBH_4$ alone (200 kJ mol^{-1} H_2).[39] Additionally, the rehydrogenation enthalpy and entropy of the $3NaBH_4$–PrF_3 composite are −18.4 kJ mol^{-1} H_2 and 33.4 J K^{-1} mol^{-1}, respectively. Compared with pure $NaBH_4$, the addition of PrF_3 decreases the dehydrogenation enthalpy by 132.5 kJ mol^{-1} H_2, which is further decreased by 7.3 kJ mol^{-1} H_2 through the addition of 5 mol% VF_3, indicating that the thermodynamics of $NaBH_4$ in those two systems are remarkably improved. It is worth noting that the asymmetric desorption and absorption may result from the difference between dehydrogenation and rehydrogenation enthalpies as shown in the $3NaBH_4$–NdF_3 composite, which arises from different reaction pathways during de/rehydrogenation.[30] The mechanisms about re-/dehydrogenation behaviors in $3NaBH_4$–PrF_3 and 5 mol% VF_3-doped $3NaBH_4$–PrF_3 composites will be proposed in the following sections.

3.2 Phase characterizations

To gain insights into the effects of PrF_3 and VF_3 on hydrogen sorption in $NaBH_4$, a series of controlled experiments and a combination of XRD, FTIR and XPS analyses were conducted to determine the chemical reactions after milling as well as different heating processes. Fig. 3 shows the results of XRD and FTIR analyses on pure $NaBH_4$, the $3NaBH_4$–PrF_3 and $3NaBH_4$–PrF_3–5 mol% VF_3 composites under different conditions.

As seen in Fig. 3(a)(A) and (B), there is no new phase present in the ball milled sample except $NaBH_4$ (JCPDS no.09-0386) and PrF_3, which indicates that a simple physical mixing of $NaBH_4$ and PrF_3 occurred after ball milling for 16 h under an argon atmosphere. As shown in Fig. 3(a)(C), after dehydrogenation at 400 °C for 1.5 h in vacuum, new compounds, NaF (JCPDS no.70-2508), PrH_2 and PrB_6, are formed accompanied with the disappearance of $NaBH_4$ and PrF_3. In contrast, a new peak appeared at a 2θ of 46°, corresponding to $NaBF_4$, but showed a smaller lattice parameter, which hinted the formation of $NaBF_{4-x}H_x$. A similar phenomenon has been observed in the $3NaBH_4$–NdF_3 composite,[30] which is associated with F^- substitution for H^- in the $NaBH_4$ lattice and has been theoretically elucidated to be an energetically favorable process.[40] After rehydrogenation at half maximum capacity, $NaBH_4$ and PrF_3 were regenerated as shown in Fig. 3(a)(D). Meanwhile, XRD patterns also revealed that $NaPrF_4$, $Na_7Pr_6F_{31}$ and PrF_4 were generated accompanied with PrH_2, PrB_6 and NaF fading away after half-rehydrogenation. In addition, the new peak at 37.6° corresponds to (200) of NaF (JCPDS no.75-0448), but shows a larger lattice parameter, indicating the formation of $NaF_{1-x}H_x$. This is resulted from the substitution of H^- for F^- in NaF.[41] After full-rehydrogenation, as shown in Fig. 3(a)(E), the diffraction intensities of $NaBH_4$ and $NaPrF_4$ are stronger, with the disappearance of PrH_2, PrB_6 and NaF. The presence of $NaPrF_4$ and $Na_7Pr_6F_{31}$ as byproducts could result in the incomplete rehydrogenation of $NaBH_4$. New phase-PrB_4 was present in the 2nd-half-dehydrogenation products as seen in Fig. 3(a)(F), which is different from the XRD pattern of Fig. 3(a)(D). However, it disappeared after 2nd-full-dehydrogenation (Fig. 3(a)(G)). The possible reactions during ball milling, dehydrogenation and rehydrogenation were further

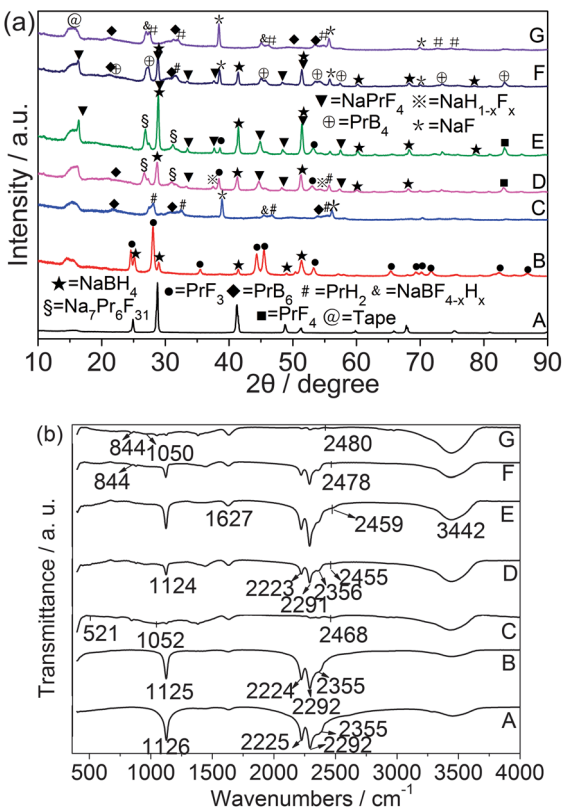

Fig. 3 XRD patterns (a) and FTIR patterns (b) of the samples: (A) pure $NaBH_4$; (B) as-milled $3NaBH_4$–PrF_3; (C) sample (B) 1st-dehydrogenated after 1.5 h at 400 °C; (D) half rehydrogenated sample (C); (E) full-rehydrogenated; (F) 2nd-half-dehydrogenated; (G) 2nd-dehydrogenated.

investigated by FTIR measurements, as shown in Fig. 3(b). In Fig. 3(b)(A) and (B), both pure $NaBH_4$ and the ball milled $3NaBH_4$–PrF_3 composite showed peaks at 2225 2292, 2355 cm^{-1} for the stretching band of B–H and a peak at 1126 cm^{-1} for the bending band located in the B–H vibration range for borohydrides. These peaks come from $NaBH_4$. In contrast, in Fig. 3(b)(C) and (G), the disappearance of the vibration of the B–H bands after 1st- and 2nd-dehydrogenation indicates the complete decomposition of $NaBH_4$. The signatures of $[BH_4]^-$ bending at 1124 cm^{-1} and $[BH_4]^-$ stretching at 2223, 2291 and 2356 cm^{-1} are clearly observed in Fig. 3(b)(D) and their vibration intensity became stronger as shown in Fig. 3(b)(E), which further confirmed the regeneration of $NaBH_4$ after rehydrogenation, agreeing well with the XRD results (Fig. 3(a)). In addition, new weak peaks around 522 and 1052 cm^{-1} were present in the 1st-dehydrogenation and 2nd-full-dehydrogenation states, as can be seen in Fig. 3(b)(C) and (G). These two peaks have also been observed in $3NaBH_4$–NdF_3[30] and the crystal $NaBF_4$-doped L-histidine.[42] They were marked as bending deformations of $[BF_4]^-$ and $[BF_4]^-$ asymmetric stretching, respectively. The formation of B–F bonds was observed by Gosalawit-Utke *et al.*[43] in the study of LiF–MgB_2 composites, which resulted from the substitution of F^- for H^- during the dehydrogenation process. Therefore, the formation of Na–B–F–H phases resulting from the substitution of F^- for H^- may also occur in the $3NaBH_4$–PrF_3 composite during the dehydrogenation process, which also agrees with the XRD result shown in Fig. 3(a). Additionally, the signature of B–B bending at 844 cm^{-1} (ref. 44) is present in the half 2nd-dehydrogenation products as shown in Fig. 3(b)(F). Moreover, a new weak peak at 2500 cm^{-1} was observed in Fig. 3(b)(C–G), which may be due to the presence of trace amounts of $Na_2[B_{12}H_{12}]$.[45] Both B and $Na_2[B_{12}H_{12}]$ were not detected in the XRD pattern due to their low volume content and/or their amorphous form. $Na_2[B_{12}H_{12}]$ is a very stable compound according to the first principles calculation,[46] which does not change during de-/rehydrogenation processes.

Among the desorption products, PrB_6 shows weak crystallization and its diffraction peaks overlapped with peaks from PrB_4 at the low diffraction angles, which makes it hard to distinguish the two phases by XRD analyses. X-ray photoelectron spectroscopy is thus applied to characterize the dehydrogenation products. The parallel XPS analyses of the dehydrogenated products of $3NaBH_4$–PrF_3 further evidenced the formation of PrB_6, as shown in Fig. 4. It is seen that the Pr 3d spectrum can be resolved into two sets of $3d_{5/2}$–$3d_{3/2}$ spin-orbit doublets at 932.2 and 952.7 eV, respectively. In B1s, two different chemical states are identified at 187.6 and 192.2 eV. The lower binding energy is the characteristic peak of PrB_6 according to the literature[47] whereas the higher one can be attributed to B_2O_3.[38] The slight oxidation of the sample is unavoidable when the sample is taken out and loaded during the XPS measurement.

Fig. 5 shows the results of XRD and FTIR analyses on the $3NaBH_4$–PrF_3–5 mol% VF_3 composite, the products of the composite after dehydrogenation and rehydrogenation, as well as the ones after half-rehydrogenation and half-dehydrogenation. Similar to what was observed in the milled $3NaBH_4$–PrF_3

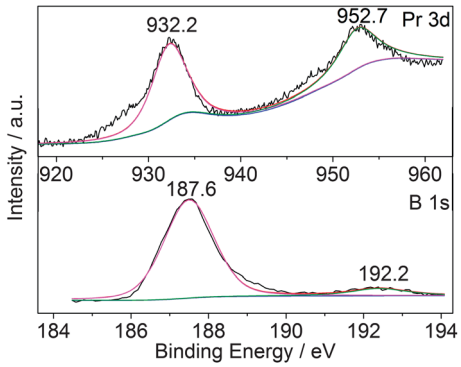

Fig. 4 Pr 3d and B 1s XPS spectra of the dehydrogenated $3NaBH_4$–PrF_3 composite.

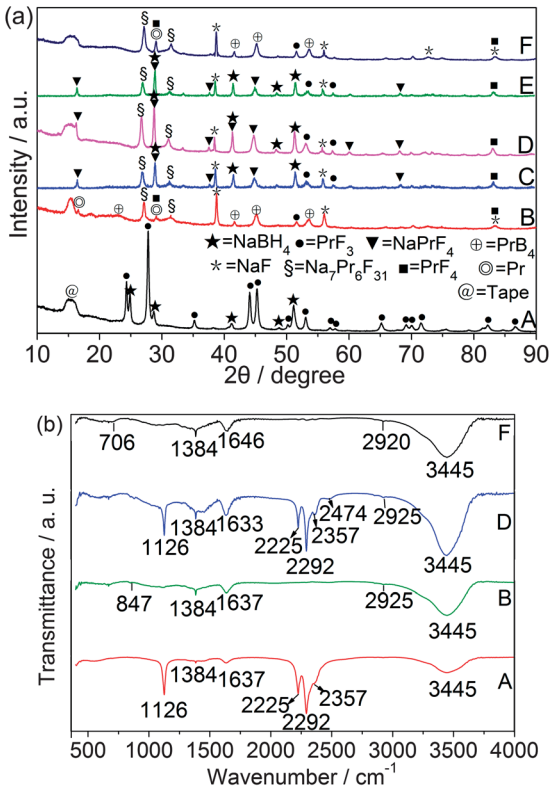

Fig. 5 XRD patterns (a) and FTIR patterns (b) of the samples: (A) as-milled $3NaBH_4$–PrF_3–5 mol% VF_3; (B) dehydrogenated after 1.5 h at 400 °C for the first time; (C) half rehydrogenated sample (B); (D) full rehydrogenated; (E) half dehydrogenated sample (D); (F) completely dehydrogenated.

composite, Fig. 5(a)(A) revealed that the milled $3NaBH_4$–PrF_3–5 mol% VF_3 composite was also a simple physical mixture. However, the XRD analysis did not detect the diffraction peaks of VF_3 due to its low content or nanocrystalline form. In addition, the lattice parameters of $NaBH_4$ (JCPDS no.09-0386) in the $3NaBH_4$–PrF_3 composite were calculated by XRD refinements as: $a = b = c = 6.162$ (2) Å, $\alpha = \beta = \gamma = 90°$ and the unit-cell volume is 234.02 $Å^3$. Whereas, the lattice parameters of $NaBH_4$ in the $3NaBH_4$–PrF_3–5 mol% VF_3 composite were calculated as: $a = b = c = 6.189$ (1) Å, $\alpha = \beta = \gamma = 90°$ and the unit-cell volume

is 237.06 Å^3. The larger lattice parameters of $NaBH_4$ in the 5 mol% VF_3 doped $3NaBH_4$–PrF_3 composite than those of $NaBH_4$ in the $3NaBH_4$–PrF_3 composite indicate that VF_3 might be dissolved into $NaBH_4$ and form a kind of solid state solution. To eliminate the possibility that the amount of VF_3 added was too low to generate any detectable diffraction intensity, a $3NaBH_4$–VF_3 composite was also prepared through ball milling and it showed only the $NaBH_4$ phase, which confirmed the formation of a solid solution. This might be the reason why VF_3 cannot be detected by XRD measurements. After dehydrogenation at 400 °C, $NaBH_4$ and PrF_3 disappeared, while Pr, NaF, PrB_4, $Na_7Pr_6F_{31}$ and PrF_4 were observed, as shown in Fig. 5(a)(B). The remaining PrF_3 indicates an incomplete reaction during the dehydrogenation process. By comparing Fig. 5(a)(C) with (D), it can be observed that, as the hydrogenation time prolonged, the peak intensities of $NaBH_4$, $NaPrF_4$ and PrF_3 gradually increased. By comparing Fig. 5(a)(E) with (F), it can be observed that, as the dehydrogenation time prolonged, the peak intensities of $NaBH_4$, $NaPrF_4$ and PrF_3 diminished gradually accompanied with the formation of Pr, NaF and PrB_4. In addition, Fig. 5(a)(C) and (E) show two identical XRD patterns. The results demonstrate the opposite reaction pathway of dehydrogenation compared to the hydrogenation one in the $3NaBH_4$–PrF_3–5 mol% VF_3 composite. As byproducts, $Na_7Pr_6F_{31}$ and PrF_4 are still present in the $3NaBH_4$–PrF_3–5 mol% VF_3 composite during the subsequent re-/dehydrogenation processes. It is worth noting that no Pr-H phase is detected by XRD in the $3NaBH_4$–PrF_3–5 mol% VF_3 composite during the dehydrogenation process, which is different from the dehydrogenation of the $3NaBH_4$–PrF_3 composite. Also, no V-relevant products were identified in any of the samples shown in Fig. 5(a).

The possible chemical changes during ball milling and de-/rehydrogenation were further investigated by FTIR measurements, as shown in Fig. 5(b). The signatures of $[BH_4]^-$ bending at 1126 cm^{-1}, and stretching at 2225, 2292 and 2357 cm^{-1} were clearly observed in ball milled and rehydrogenated samples, as shown in Fig. 5(b)(A) and (D). This confirmed the formation of $NaBH_4$ after rehydrogenation. In Fig. 5(b)(B) and (F), no vibration bands of B–H coming from the $[BH_4]^-$ ligand were detected after dehydrogenation at 400 °C for 1.5 h, indicating a complete decomposition of $NaBH_4$ in $3NaBH_4$–PrF_3–5 mol% VF_3. And the peaks corresponding to B–B bending at 847, 2950 and 706 cm^{-1} according to the literature[44] were present in both first dehydrogenated and second dehydrogenated products.

The peaks located at around 1630 and 3445 cm^{-1} belong to H–O–H for bending bands and O–H for stretching bands, respectively, as shown in Fig. 3(b) and 5(b). This results from the unavoidable moisture absorption of the sample during the FTIR measurements.

XPS analyses were used to further distinguish the Pr-B phases in dehydrogenated products, as well as to identify the V-containing phase in the de-/rehydrogenated $3NaBH_4$–PrF_3–5 mol% VF_3 composite. The results are shown in Fig. 6. It is seen that the Pr 3d spectrum shows two sets of $3d_{5/2}$–$3d_{3/2}$ spin-orbit doublets at 931.2 and 952.7 eV, which is different from the spectrum of PrB_6 shown in Fig. 4. The peak fitting reveals that the B 1s peak in dehydrogenated products of the $3NaBH_4$–PrF_3–

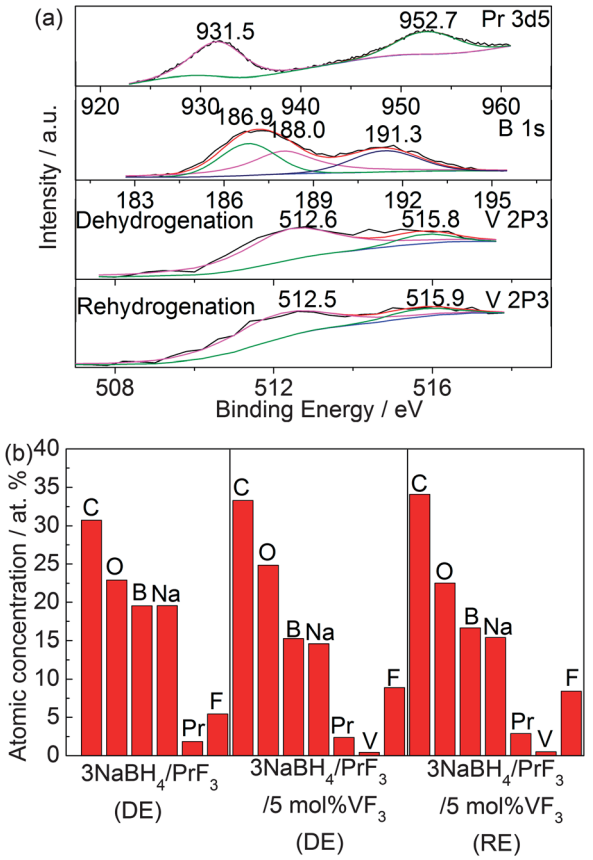

Fig. 6 (a): XPS spectra of: Pr 3d, B 1s and V 2p in the $3NaBH_4$–PrF_3–5 mol% VF_3 sample in the dehydrogenated state (heating for 1.5 h at 400 °C for the first time); as well as V 2p in the full rehydrogenated state after dehydrogenation; (b) atomic composition for binary and ternary systems in the dehydrogenation state, as well as the ternary system in the rehydrogenation state after dehydrogenation.

5 mol% VF_3 composite has three different contributions: PrB_4, VB_2 and B_2O_3 which appear in B 1s at 188.0, 186.9 and 191.3 eV according to the literature,[38,48] respectively. For the dehydrogenated sample of the $3NaBH_4$–PrF_3–5 mol% VF_3 composite, the V 2p spectrum can be resolved into two spin–orbit-split doublets at 512.6 (V $2p_{3/2}$) and 515.8 eV. The higher binding energy contribution is the characteristic of oxidized vanadium, whereas the second one (512.6 eV) can be attributed to VB_2 according to the literature.[48] For the rehydrogenated sample of the $3NaBH_4$–PrF_3–5 mol% VF_3 composite, V 2p binding energies are 512. 5 and 515.9 eV, which are all in the range of the binding energy of VB_2 and oxidized vanadium, respectively. According to the XPS analyses, VF_3 has completely reacted with $NaBH_4$ upon heating at 400 °C, resulting in the formation of VB_2. The formed VB_2 maintains its phase stability in the subsequent de-/rehydrogenation processes. Fig. 6(b) shows that the atomic concentration of V is only 0.4 at.%, which is 1/35 of Na at.%. Compared with the initial atomic concentration of V (1/15 of Na at.%), the decreased atomic concentration of V on the surface upon de-/rehydrogenation indicates the migration of part of V atoms/ions towards bulk, where they favor heterogeneous reactions at the interface of reactants according to the literature.[49] The higher atomic concentration of Pr in the

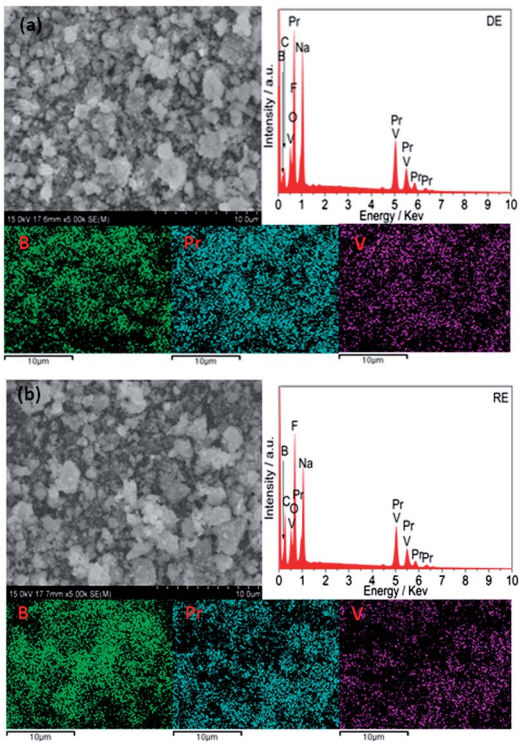

Fig. 7 Typical SEM images, the corresponding EDS spectra and elemental distribution maps of the $3NaBH_4$–PrF_3–5 mol% VF_3 composite after 1st dehydrogenation (a) and 1st rehydrogenation (b).

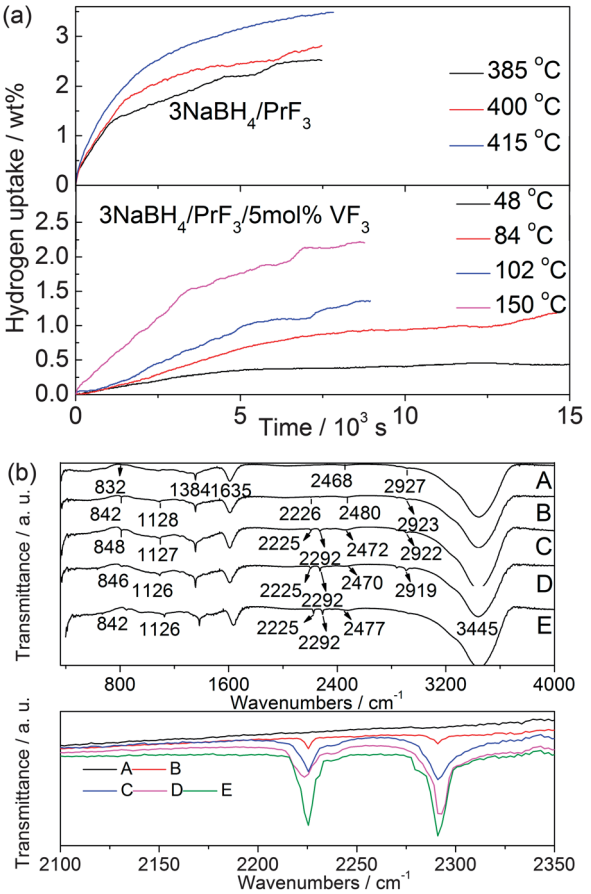

Fig. 8 (a) Isothermal profiles of rehydrogenation of: $3NaBH_4$–PrF_3 samples at 385, 400 and 415 °C under 3.2 MPa; $3NaBH_4$–PrF_3–5 mol% VF_3 samples at 48, 84, 102 and 150 °C under 3.2 MPa; (b): (up): FTIR spectra of $3NaBH_4$–PrF_3–5 mol% VF_3 samples: (A) dehydrogenated completely for the first time at 430 °C under vacuum; after rehydrogenation under 3.2 MPa of hydrogen at: (B) 48 °C for 6 h; (c) 84 °C for 4 h; (D) 102 °C for 2.6 h; (E) 150 °C for 2.6 h; (bottom): the enlargement of (up) from the wavenumber of 2100 to 2350 cm^{-1}.

dehydrogenated $3NaBH_4$–PrF_3–5 mol% VF_3 composite than the dehydrogenated $3NaBH_4$–PrF_3 composite indicates again the favorable effect of VB_2 in improving the heterogeneous nucleation of PrB_4. A similar phenomenon has been observed in the study of Ti-based compound doped $LiBH_4$–MgH_2.[50]

The SEM micrographs, EDS spectra, and elemental distribution maps recorded from the de-/rehydrogenated samples of $3NaBH_4$–PrF_3–5 mol% VF_3 are given in Fig. 7. SEM images in Fig. 7(a) and (b) reveal that the de-/rehydrogenated composites are composed of irregular shaped particles having sizes ranging from tens of nm to several μm. The corresponding EDS spectra show peaks mainly belonging to Na, B, Pr, V and F. C and O can be also detected. They may come from contaminations or conductive tape below the composite powders. The elemental distribution maps of B, Pr and V show that these 3 elements are distributed fairly homogenous in both dehydrogenated and rehydrogenated composite samples.

3.3 De-/rehydriding kinetics for $3NaBH_4$–PrF_3 without and with VF_3-doping

The effects of PrF_3 and VF_3 on the hydrogen sorption reversibility in $NaBH_4$ were further investigated. The rehydrogenation behaviors of the $3NaBH_4$–PrF_3 composite were examined under 3.2 MPa of hydrogen at 385 °C, 400 °C and 415 °C, as shown in Fig. 8(a)-up. All the measurements were carried out after the initial dehydrogenation at 420 °C for 2 h under vacuum. The dehydrogenated samples showed good absorption kinetics: the hydrogen uptake reached up to 3.48 wt% in 2 h at 415 °C, which was fairly close to the theoretical hydrogen content of the composite. While at 385 and 400 °C, the sample can absorb 2.53 wt% and 2.81 wt% of hydrogen in 2 h, respectively. The effect of VB_2 on reversible hydrogenation of the $3NaBH_4$–PrF_3–5 mol% VF_3 composite was subsequently investigated by several designed experiments conducted at relatively low temperatures. Fig. 8(a)-down shows the isothermal rehydrogenation behaviors of dehydrogenated $3NaBH_4$–PrF_3–5 mol% VF_3 samples examined under 3.2 MPa of hydrogen pressure at 48 °C, 84 °C, 102 °C and 150 °C, respectively. As indicated in Fig. 8(a)-down, the sample of dehydrogenated $3NaBH_4$–PrF_3–5 mol% VF_3 can absorb 2.23 wt% of hydrogen in 2.4 h at 150 °C. The hydrogen absorption capacity varies with the temperature, reaching 1.36 wt% in 2.4 h at 102 °C, and 1.19 wt% in 4 h at 84 °C. Even at 48 °C, the sample can still absorb 0.43 wt% in 4 h, which means that 12.3 wt% of $NaBH_4$ in the composite can be regenerated under this condition. The rehydrogenated samples obtained at low temperatures (48, 84, 102, 150 °C) as well as the dehydrogenated sample were further subjected to FTIR examinations, as shown in Fig. 8(b). Fig. 8(b)-down shows the enlargement of (b)-up from the wavenumber of 2100 to 2350 cm^{-1}. The signatures

of $[BH_4]^-$ bending at 1126 cm^{-1} and stretching at 2225 and 2292 cm^{-1} were obtained in all the rehydrogenated samples (Fig. 8(b)), indicating the regeneration of $NaBH_4$. The peak intensities of $[BH_4]^-$ stretching increase with increasing temperature (Fig. 8(b)-down), showing the increasing amount of regenerated $NaBH_4$ with increasing temperature. In addition, a new transmittance emerges at around 2470 cm^{-1}, which agrees well with the B–H vibration of $[B_{12}H_{12}]^{2-}$. The presence of $[B_{12}H_{12}]^{2-}$ containing compounds may be one of the reasons resulting in the incomplete reversibility in the $3NaBH_4$–PrF_3–5 mol% VF_3 composite.

To gain more insights into the dehydrogenation behaviors, the temperature-programmed-desorption (TPD) data of the two composites were collected at a constant heating rate (3 °C min^{-1}), as shown in Fig. 9(a). The onset dehydrogenation temperature of pure $NaBH_4$ is around 473 °C in vacuum,[30] while after PrF_3 addition, the onset dehydrogenation temperature is lowered down to around 110 °C and the peak dehydrogenation temperature is 415 °C. On further doping with 5 mol% of VF_3, interestingly, a two-step dehydrogenation was observed. The first dehydrogenation step starts at around 46 °C, which is 64 °C lower than that for the $3NaBH_4$–PrF_3 composite. The fastest kinetics of the first dehydriding step in the ternary composite is achieved at around 210 °C, and is completed at 290 °C, which may result from the reaction between $NaBH_4$ and the VF_3 additive. Meanwhile, the onset temperature for the second dehydrogenation step of the ternary composite is around 300 °C, the fastest desorption rate is achieved at around 390 °C and is completed at around 405 °C, which may be due to the reaction between $NaBH_4$ and PrF_3. However, in the range from 300 °C to 390 °C, the slope of the dehydrogenation curve for $3NaBH_4$–PrF_3–5 mol% VF_3 is obviously sharper than the slope of the dehydrogenation curve for the $3NaBH_4$–PrF_3 composite, indicating a higher dehydrogenation rate in the ternary composite than that in the binary composite. After heating, a total hydrogen release of 3.52 wt% and 3.59 wt% was achieved (both are 99.7% of their theoretical hydrogen capacity) in the $3NaBH_4$–PrF_3 composite and in the $3NaBH_4$–PrF_3–5 mol% VF_3 composite, respectively.

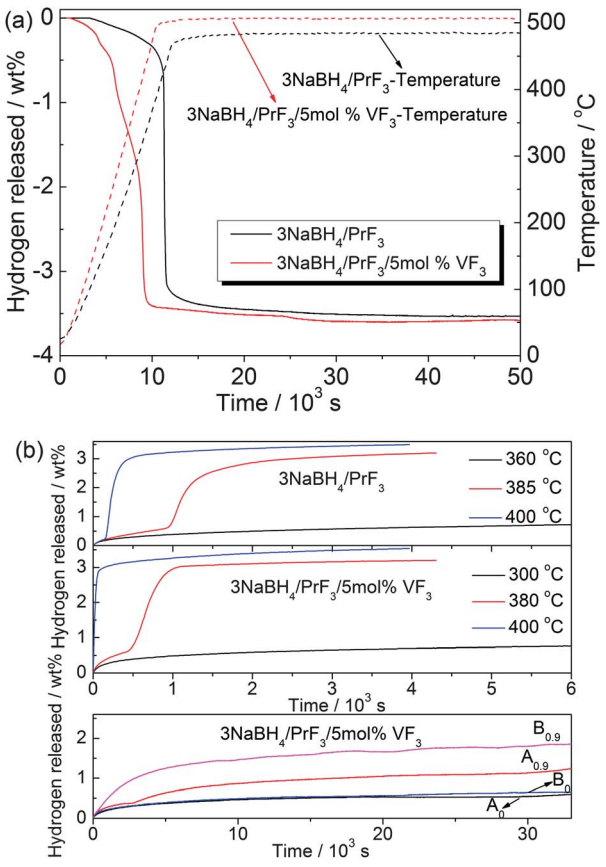

Fig. 9 (a) Temperature-programmed-desorption (TPD) profiles of $3NaBH_4$–PrF_3 without and with 5 mol% VF_3-doping. The heating rate is 3 °C min^{-1}; (b) isothermal profiles of: first dehydrogenation of: $3NaBH_4$–PrF_3 samples at 360, 385 and 400 °C; $3NaBH_4$–PrF_3–5 mol% VF_3 samples at 300, 380 and 400 °C; as well as second dehydrogenation of $3NaBH_4$–PrF_3–5 mol% VF_3 samples at 84 (A) and 100 °C (B) under 0 and 0.9 MPa, respectively.

The isothermal dehydrogenation behaviors of the $3NaBH_4$–PrF_3 composite were further examined at 360 °C, 385 °C and 400 °C, and those of the $3NaBH_4$–PrF_3–5 mol% VF_3 composite samples were also examined at 300 °C, 380 °C and 400 °C for comparison, as shown in Fig. 9(b). Fig. 9(b)-up shows that the $3NaBH_4$–PrF_3 composite can rapidly release 3 wt% of hydrogen within 7 minutes at 400 °C, which is much faster than pure $NaBH_4$ under the same condition.[30] Though the hydrogen desorption rate of the $3NaBH_4$–PrF_3 composite lowers down when the temperature reduces to 360 °C, there is still 0.73 wt% of hydrogen released after 1.6 h. Fig. 9(b)-middle shows that the hydrogen released from the $3NaBH_4$–PrF_3–5 mol% VF_3 composite reaches up to 3 wt% within 2 minutes at 400 °C and 17 minutes at 380 °C. This clearly shows the effect of VF_3 addition on the improvement of dehydrogenation kinetics in the $3NaBH_4$–PrF_3 system. The dehydrogenation kinetics shown in Fig. 9(b)-up and middle displayed a good agreement with that in Fig. 9(a). However, there exists an incubation period in both the $3NaBH_4$–PrF_3 and $3NaBH_4$–PrF_3–5 mol% VF_3 composites when dehydrogenated at 385 and 380 °C, which might be caused by a necessary nucleation and growth process of an intermediate, or some other factors, such as phase distribution, particle and crystallite size, *etc.* A similar phenomenon has been observed in other borohydride containing systems.[49,51,52] Under identical measurement conditions, the duration of incubation becomes shorter upon adding VF_3, indicating its effect on further promoting the dehydrogenation of $NaBH_4$.

The isothermal desorption profiles for the second desorption cycle at 84 and 100 °C (against back pressures of 0 MPa and 0.9 MPa) were collected to further study the cyclic properties of the $3NaBH_4$–PrF_3–5 mol% VF_3 composite at low temperatures, as shown in Fig. 9(b)-down. Before each desorption test, samples were first completely dehydrogenated at 420 °C and then rehydrogenated under 3.2 MPa for 10 h at desired temperatures. Fig. 9(b)-down shows that after rehydrogenation at 84 and 100 °C for 10 h, the samples can release 0.54 wt% and 0.59 wt% of hydrogen after heating for 5 h, and 0.61 wt% and 0.67 wt% of hydrogen in total in 8.6 h without back pressure. However, the 100 °C-rehydrogenated sample is capable of desorbing more than 1.67 wt% hydrogen after heating for 5 h,

and 1.87 wt% hydrogen in the total measurement time at 100 °C against a back pressure of 0.9 MPa, indicating a dramatically accelerated desorption kinetics under back pressures. Even at 84 °C against a back pressure of 0.9 MPa, the hydrogen desorption can reach up to 1.17 wt% after heating for 5 h, and 1.26 wt% in the total measurement duration. The above results clearly revealed the enhancement in hydrogen sorption arising upon adding VF_3 in de-/rehydrogenation cycles. In particular, the $3NaBH_4$–PrF_3–5 mol% VF_3 composite can reversibly absorb and desorb around 1.2 wt% of hydrogen at 84 °C, which is fairly close to the storage capacity of the industrialized $LaNi_5$ intermetallic compound (1.37 wt%). To the best of our knowledge, such a pronounced property improvement in both dehydrogenation and rehydrogenation under moderate conditions has never been achieved in metal borohydride containing systems.[19,20,38,53–58] Table 3 summarizes re-/dehydrogenation temperatures and hydrogen pressures needed for rehydrogenation in some metal borohydride containing reversible systems. The lowest onset dehydriding and rehydriding temperatures are achieved in the $3NaBH_4$–PrF_3–5 mol% VF_3 composite in the present study.

The results obtained from Fig. 8(a)-down and Fig. 9(b)-down agree well with the theory proposed by U. Bosenberg, in which the effect of the improved kinetics by additives is sustainable upon further cycling due to the formation of nanostructured additives as well as their location at the interfaces during cycling.[33,52]

3.4 Mechanisms of re-/dehydrogenation in $3NaBH_4$–PrF_3 without and with VF_3-doping

Fig. 10 shows the XRD patterns of $3NaBH_4$–PrF_3 after dehydrogenation under vacuum at 150, 350 and 410 °C. In Fig. 10, besides the presence of $NaBH_4$ and PrF_3, a weak peak of NaF appeared upon heating at 150 °C, indicating that the reaction has already occurred under this temperature.

In contrast, PrH_2 and PrB_6 were visible after the temperature reached 350 °C, together with the disappearance of $NaBH_4$ and PrF_3. After heating at 410 °C, the diffraction analysis showed a further increase in peak intensities of NaF, PrH_2 and PrB_6. In addition, $NaBF_{4-x}H_x$ was also observed after the sample was heated to 350 and 410 °C, which agreed well with Fig. 3(a). The formation of PrH_2 and $NaBF_{4-x}H_x$ may result from the interchange of F^- for H^- since the ionic radii of F^- and H^- are fairly close to each other.[43] According to the literature,[30] the following reaction might take place at the early stage of first dehydrogenation in the $3NaBH_4$–PrF_3 composite:

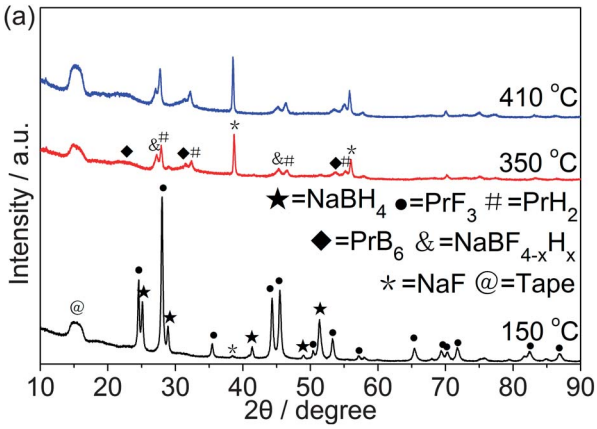

Fig. 10 XRD patterns of the $3NaBH_4$–PrF_3 composite after 1st-dehydrogenation at 150, 350 and 410 °C.

$$3NaBH_4 + (4-x)\,PrF_3 = 3NaBH_xF_{4-x} + (4-x)\,PrH_2 + (2-x/2)H_2. \quad (3)$$

Suppose $x = 1$, reaction (3) could give a hydrogen release of about 0.42 wt% in the $3NaBH_4$–PrF_3 composite, which agrees with the fact that a small amount of hydrogen is released at low temperatures, as shown in Fig. 9(a), as well as the appearance of B–F bonds shown in Fig. 3. PrH_2 formed and dispersed homogeneously in the system, which might act as a catalyst for the dehydrogenation of the $3NaBH_4$–PrF_3 composite during the subsequent dehydrogenation processes.[29,30] The main reaction pathway of the first dehydrogenation in $3NaBH_4$–PrF_3 can be deduced based on the XRD analyses as follows:

Table 3 Some parameters for hydrogen sorption in borohydride containing hydrogen storage systems

System	Onset dehydrogenation temperature/°C	Rehydrogenation temperature/°C	Rehydrogenation pressure/MPa	References
$NaBH_4$–MgH_2–TiF_3	260	600	4	54
$CaBH_4$–NbF_5	225	350	14.5	57
$LiAlH_4$–MgH_2–$LiBH_4$–TiF_3	60	400	4	56
$CaBH_4$–MgF_2	280	330	13	59
$NaBH_4$–$LiAlH_4$–TiF_3	60	600	10	55
$NaBH_4$–TiF_3	300	500	5.5	20
$LiBH_4$–TiF_3	100	350	10	38
$NaBH_4$ confined in nanoporous carbon	220	325	6	19
Li–Mg–B–H + TiF_3	309	350	7.5	58
$3NaBH_4$–YF_3	423	350	3.5	31
$3NaBH_4$–NdF_3	80	300	3.16	30
$3NaBH_4$–PrF_3–5%VF_3	46	48	3.2	This work

$$6NaBH_4 + 2PrF_3 = 6NaF + PrH_2 + PrB_6 + 11H_2. \quad (4)$$

For the rehydrogenation processes of the decomposed $3NaBH_4$–PrF_3 system, as shown in Fig. 3(a), $NaBH_4$, PrF_3, $NaPrF_4$ and $Na_7Pr_6F_{31}$ were clearly identified together with a small amount of PrF_4 and residual NaF in the half-rehydrogenated sample at 400 °C (Fig. 3 (a)(D)). After full- rehydrogenation at 400 °C (Fig. 3 (a)(E)), the diffraction analysis shows a further increase in peak intensities of $NaBH_4$ and $NaPrF_4$ and a decrease in the PrF_3 peak intensity, accompanied with the disappearance of NaF. However, PrF_4 as a byproduct was detected by the XRD pattern in both half and full-rehydrogenated samples, and it could combine with NaF contributing to the formation of $Na_7Pr_6F_{31}$ (space group $R\bar{3}$) since the radius ratio of Na^+/Pr^{4+} is 1.09.[60] R. E. Thoma reported that $M_7RE_6F_{31}$ with the space group $R\bar{3}$ (7MF.6ReF$_4$) (M = alkali metal, RE = rare earth metal) might form when the M^+/Re^{4+} cation radius ratio lies between 0.99 and 1.68.[60] Compared with Fig. 3 (b)(D) and (E), no other new peaks were detected but there was an increase in the bending energy intensity of $[BH_4]^-$ coming from $NaBH_4$. According to XRD measurements shown in Fig. 3(a), the dehydrogenated products of $3NaBH_4$–PrF_3, namely, the combination of NaF, PrH_2 and PrB_6, form the reversible hydrogen storage mixture.

Based on the XRD and FTIR data shown in Fig. 3, the major rehydrogenation pathway could be proposed as follows:

$$8NaF + PrH_2 + PrB_6 + 11H_2 = 6NaBH_4 + 2NaPrF_4. \quad (5)$$

The rehydrogenation reaction in the $3NaBH_4$–PrF_3 composite is very similar to what is observed in the $3NaBH_4$–NdF_3 system.[30]

According to Fig. 3(a)(E)(F) and (b)(E)(F), the 1st- and 2nd-dehydrogenation processes may take different pathways. The reactions taking place during the 2nd-dehydrogenation could be described as follows:

$$NaPrF_4 = NaF + PrF_3, \quad (6)$$

$$6NaBH_4 + 2PrF_3 = 6NaF + PrB_4 + 2B + PrH_2 + 11H_2. \quad (7)$$

As the reaction proceeded, PrB_4 and B eventually disappeared accompanied with the formation of PrB_6 and PrH_2. Boron could promote the transformation of PrB_4 to PrB_6.[61] The formation of PrB_4 and B as intermediate products during the dehydrogenation process is probably the major reason why the dehydrogenation enthalpy value is higher than that of rehydrogenation.

For the dehydrogenation of the 5 mol% VF_3-doped $3NaBH_4$–PrF_3 composite, though there is no V-containing phase detected in the XRD pattern as shown in Fig. 5(a), VB_2 is revealed by the XPS analysis shown in Fig. 6, indicating that a reaction has taken place between $NaBH_4$ and VF_3. Both DSC and TPD analyses revealed a two-step hydrogen release during the first dehydrogenation of the $3NaBH_4$–PrF_3–5 mol% VF_3 composite. It is seen that Pr, PrB_4 and NaF formed after dehydrogenation at 400 °C for 2 h under vacuum as seen in Fig. 5(a)(B). Therefore, it can be deduced that the first dehydrogenation step involves the reaction between $NaBH_4$ and VF_3 which produces 20% of hydrogen of the theoretical content according to the following reaction:

$$3NaBH_4 + VF_3 = 3NaF + VB_2 + B + 6H_2. \quad (8)$$

This step could release about 0.7 wt% of hydrogen, which is consistent with the TPD measurement shown in Fig. 9(a).

In a study on the chemical state and distribution of Zr- and V-based additives in reactive hydride composites, U. Bosenberg *et al.*[33] reported that transition metal borides are formed from the transition metal based additives, which were stable, and present as fine distributed nanoparticles in the whole composite. Similar to their observations, the stable VB_2 may also be present as fine nanoparticles and distribute in the mixture of $NaBH_4$ and PrF_3 during the dehydrogenation process.

During the subsequent dehydrogenation process, VB_2 will act as a catalyst to promote the dehydrogenation of the rest of the composite. According to Fig. 5(a)(B) and (b)(B), the second step of the first dehydrogenation can be therefore described as:

$$6NaBH_4 + 2PrF_3 \xrightarrow{VB_2} 6NaF + PrB_4 + 2B + Pr + 12H_2. \quad (9)$$

It has been established that the nucleation of MgB_2 plays a key role in the onset of hydrogen desorption in $LiBH_4$–MgH_2 systems, while transition-metal borides may act as heterogeneous nucleation sites for MgB_2. In the present case, VB_2 may also provide heterogeneous nucleation sites for the formation of PrB_4, which favors hydrogen desorption, resulting in the microstructure refinement with improved desorption and absorption kinetics (Fig. 8(a)-down).

XPS analyses show that VB_2 well maintains its phase stability in the subsequent de-/rehydrogenation processes, suggesting that VB_2 is not any more a reagent involved in the re-/dehydrogenation cycles but acts as a catalyst. Therefore, based on the results shown in Fig. 5 (a)(C), (a)(D) and (b)(D), the main rehydrogenation pathway for the $3NaBH_4$–PrF_3–5 mol% VF_3 composite could be proposed as:

$$8NaF + PrB_4 + 2B + Pr + 12H_2 \xrightarrow{VB_2} 6NaBH_4 + 2NaPrF_4, \quad (10)$$

which is slightly different from the rehydrogenation reaction in the $3NaBH_4$–PrF_3 composite given in formula (5). XRD and FTIR analyses confirm that the second dehydrogenation takes exactly the reverse reaction pathway of the first rehydrogenation in the $3NaBH_4$–PrF_3–5 mol% VF_3 composite without the formation of intermediate products. This might be the main reason why the hysteresis is postponed in the $3NaBH_4$–PrF_3–5 mol% VF_3 composite.

The efficiency of a catalyst depends not only on its intrinsic activity, but also on its distribution states for heterogeneously catalyzed reactions.[62] In the present case, VB_2 has a favourable dispersed state, a role played as the heterogeneous nucleation sites for PrB_4, as well as intrinsic activity, all of which improve

significantly the hydrogen sorption kinetics in the $3NaBH_4$–PrF_3 system, especially at lower temperatures.

It is worth noting that the dehydrogenation kinetics of the $3NaBH_4$–PrF_3–5 mol% VF_3 composite at low temperatures is favoured by the hydrogen back pressure, as shown in Fig. 9(b)-down. Calculated using the HSC chemistry program,[63] the Gibbs free energies of the reaction: $Pr + H_2 = PrH_2$ are -147.7 kJ mol^{-1} at 80 °C, and -144.7 kJ mol^{-1} at 100 °C, respectively. This implies that a spontaneous reaction should take place between Pr (one of the dehydrogenation products) and H_2 to yield Pr-H phases at these temperatures under hydrogen pressures. Indeed, it has been reported by Shim *et al.*[64] that the hydrogen back pressure can accelerate the dehydrogenation rate in hydrogen storage composites containing both borohydrides and metal hydrides by promoting the formation of metal borides, such as in the $4LiBH_4$–YH_3 and $6LiBH_4$–CeH_2 systems. Considering the above, it is possible that the transient presence of Pr-H phases may occur during dehydrogenation under hydrogen pressures, which promotes the formation of PrB_4 and therefore improves dehydrogenation kinetics.

4. Conclusions

It is demonstrated in the present work that the $3NaBH_4$–PrF_3 composite is a reversible hydrogen storage system. After doping with VF_3, the ternary system ($3NaBH_4$–PrF_3–5 mol% VF_3 composite) shows much improved hydrogen sorption thermodynamic and kinetic properties. The de-/rehydrogenation behaviors and related phase transitions, as well as the mechanisms of hydrogen desorption and absorption in the $3NaBH_4$–PrF_3 composite without and with VF_3 addition have been investigated in detail by means of TG/DSC/MS, XRD, PCT, TPD, XPS and FTIR techniques. The main results are summarized as follows:

1. The $3NaBH_4$–PrF_3 composite is verified to be a reversible hydrogen storage system. Its dehydrogenation and rehydrogenation enthalpies are determined to be 67.5 and -18.4 kJ mol^{-1} H_2, respectively. The large difference in de-/rehydrogenation enthalpies results from the different reaction pathways of de-/rehydrogenation, which accounts for the hysteresis phenomenon observed in the $3NaBH_4$–PrF_3 composite.

2. The onset dehydriding temperature of the $3NaBH_4$–PrF_3 composite is 110 °C in vacuum. The composite releases about 3.01 wt% hydrogen within 7 min at 400 °C and is able to absorb about 3.48 wt% (98.58% of the theoretical value) hydrogen in 2 h at 415 °C under 3.2 MPa hydrogen pressure.

3. The addition of VF_3 changes the de-/rehydrogenation reactions in the $3NaBH_4$–PrF_3 composite. A two-step reaction takes place during the first dehydrogenation process of the $3NaBH_4$–PrF_3–5 mol% VF_3 composite. That is, VF_3 first reacts with $NaBH_4$ to produce VB_2, then VB_2 serves as a catalyst for the reaction between $NaBH_4$ and PrF_3 to produce NaF, Pr, PrB_4 and B. These products are different from the dehydrogenation products of undoped $3NaBH_4$–PrF_3 (*e.g.* NaF, PrH_2, PrB_6). During subsequent re-/dehydrogenation cycles, VB_2 maintains its phase stability and acts as heterogeneous nucleation sites for PrB_4, thereby improving the hydrogen sorption kinetics. As the dehydrogenation reaction takes the reverse pathway of the rehydrogenation reaction after first dehydrogenation, the hysteresis phenomenon is postponed in the $3NaBH_4$–PrF_3–5 mol% VF_3 composite.

4. In the 5 mol% VF_3 doped $3NaBH_4$–PrF_3 composite, the onset dehydrogenation temperature is lowered down to 46 °C in vacuum. The composite is able to release 3.01 wt% hydrogen in 2 min at 400 °C. In addition, the dehydrogenation enthalpy decreases to 60.2 kJ mol^{-1} H_2, 7.5 kJ mol^{-1} H_2 lower than that of the undoped $3NaBH_4$–PrF_3.

5. Through VF_3 addition, it is possible to regenerate $NaBH_4$ in the dehydrogenated $3NaBH_4$–PrF_3–5 mol% VF_3 composite at fairly low temperatures. The onset rehydrogenation temperature for $NaBH_4$ in the composite can be as low as 48 °C. At 84 °C, the reversible hydrogen sorption capacity of the $3NaBH_4$–PrF_3–5 mol% VF_3 composite can reach up to ~1.2 wt%. In addition, the hydrogen back pressure favors the dehydrogenation kinetics of the composite at low temperatures. According to a series of designed experiments and results of phase analyses, the remarkably improved de-/rehydrogenation properties of the $3NaBH_4$–PrF_3–5 mol% VF_3 composite can be mainly ascribed to the combined effects from the formation of active Pr-B species, the presence of VB_2 as the catalyst and the functional characters of the F^- anion.

Acknowledgements

Prof. Zou would like to thank the support from the Science and Technology Committee of Shanghai under nos 10JC1407700 and 11ZR1417600, and 'Pujiang' project (no. 11PJ1406000). This work is partly supported by the Research Fund for the Doctoral Program of Higher Education of China (no. 20100073120007) and by the Shanghai Education Commission (no. 12ZZ017).

References

1 L. Schlapbach and A. Zuttel, *Nature*, 2001, **414**, 353–358.
2 J. Yang, A. Sudik, C. Wolverton and D. J. Siegel, *Chem. Soc. Rev.*, 2010, **39**, 656–675.
3 W. Grochala and P. P. Edwards, *Chem Rev.*, 2004, **104**, 1283–1315.
4 A. Zuttel, A. Borgschulte and S. I. Orimo, *Scr. Mater.*, 2007, **56**, 823–828.
5 Y. Nkamori, H. W. Li, K. Miwa, S. Towata and S. Orimo, *Mater. Trans.*, 2006, **47**, 1898–1901.
6 S. Orimo, Y. Nakamori and A. Zuttel, *Mater. Sci. Eng., B*, 2004, **108**, 51–53.
7 R. Cerny, Y. Filinchuk, H. Hagemann and K. Yvon, *Angew. Chem., Int. Ed.*, 2007, **46**, 5756–5767.
8 S. Orimo, Y. Nakamori, J. R. Eliseo, A. Zuttel and C. M. Jensen, *Chem. Rev.*, 2007, **107**, 4111–4132.
9 Y. Filinchuk, D. Chernyshov and V. Dmitrev, *Z. Kristallogr.*, 2008, **223**, 649–659.
10 https://www.eecbg.energy.gov/hydrogenandfuelcells/storage/pdfs/targets_onboard_hydro_storage.pdf.
11 H. I. Schlesinger, H. C. Brown, A. E. Finholt, J. R. Gilbrath, H. R. Hoekstra and E. K. Hyde, *J. Am. Chem. Soc.*, 1953, **75**, 215–219.

12 D. R. Stull and H. Prophet, *JANAF Thermochemical Tables*, U.S.Department of Commerce, Washington, DC, 1985, Cp Fitted by CRCT, Montreal.
13 D. Stasinevich and G. Egorenko, *Zh. Neorg. Khim.*, 1968, **13**, 654–658.
14 P. Martelli, R. Caputo, A. Remhof, P. Mauron, A. Borgschulte and A. Zuttel, *J. Phys. Chem. C*, 2010, **114**, 7173–7177.
15 C. Pistidda, G. Barkhordarian, A. Rzeszutek, S. Garroni, C. B. Minella, M. D. Baro, P. Nolis, R. Bormann, T. Klassen and M. Dornheim, *Scr. Mater.*, 2011, **64**, 1035–1038.
16 S. Garroni, C. Pistidda, M. Brunelli, G. B. M. Vaughan, S. Surinach and M. D. Baro, *Scr. Mater.*, 2009, **60**, 1129–1132.
17 C. Pistidda, S. Garroni, C. B. Minella, F. Dolci, T. R. Jensen, P. Nolis, U. Bosenberg, Y. Cerenius, W. Lohstroh, M. Fichtner, M. D. Baro, R. Bormann and M. Dornheim, *J. Phys. Chem. C*, 2010, **114**, 21816–21823.
18 C. Milanese, S. Garroni, A. Girella, G. Mulas, V. Berbenni, G. Bruni, S. Surinach, M. D. Baro and A. Marini, *J. Phys. Chem. C*, 2011, **115**, 3151–3162.
19 P. Ngene, R. van den Berg, M. H. W. Verkuijlen, K. P. de Jong and P. E. de Jongh, *Energy Environ. Sci.*, 2011, **4**, 4108–4115.
20 J. F. Mao, Z. P. Guo, I. P. Nevirkovets, H. K. Liu and S. X. Dou, *J. Phys. Chem. C*, 2012, **116**, 1596–1604.
21 S. A. Jin, J. H. Shim, Y. W. Cho, K. W. Yi, O. Zabara and M. Fichtner, *Scr. Mater.*, 2008, **58**, 963–965.
22 K. E. Spear, Phase behavior and related properties of rare earth borides, in *Phase Diagrams: Materials Science and Technology*, ed. A. M. Alper, Academic Press, 1976, vol. 4, ch. 2, pp. 91–159.
23 K. E. Spear, Rare Earth-Boron phase Equilibria, in *Boron and Refractory Borides*, ed. V. I. Matkovich, Springer-Vedag, New York, 1977, pp. 439–456.
24 B. T. Matthias, T. H. Geballe, K. Andres, E. Corenzwit, G. W. Hull and J. P. Maita, *Science*, 1968, **159**, 530.
25 S. V. Meschel and O. J. Kleppa, *J. Alloys Compd.*, 1995, **226**, 243–247.
26 I. Barin, *Thermochemical Data of Pure Substances*, VCH Verlags Gesellschaft, Weinheim, 1993.
27 A. V. Blinder, S. P. Goridienko, V. Marek and V. B. Muratov, *Powder Metall. Met. Ceram.*, 1997, **36**, 409–412.
28 T. Sato, K. Miwa, Y. Nakamori, K. Ohoyama, H. W. Li, T. Noritake, M. Aoki, S. I. Towata and S. I. Orimo, *Phys. Rev. B: Condens. Matter Mater. Phys.*, 2008, **77**, 1–8.
29 P. Mauron, M. Bielmann, A. Remhof, A. Zuttel, J. H. Shim and Y. W. Cho, *J. Phys. Chem. C*, 2010, **114**, 16801–16805.
30 L. N. Chong, J. X. Zou, X. Q. Zeng and W. J. Ding, *J. Mater. Chem. A*, 2013, **1**, 3983–3391.
31 J. X. Zou, L. J. Li, X. Q. Zeng and W. J. Ding, *Int. J. Hydrogen Energy*, 2012, **37**, 17118–17125.
32 L. C. Yin, P. Wang, X. D. Kang, C. H. Sun and H. M. Cheng, *Phys. Chem. Chem. Phys.*, 2007, **9**, 1499–1502.
33 U. Bosenberg, U. Vainio, P. K. Pranzas, J. M. B. von Colbe, G. Goerigk, E. Welter, M. Dornheim, A. Schreyer and R. Bormann, *Nanotechnology*, 2009, **20**, 1–9.
34 A. Zaluska and L. Zaluski, *J. Alloys Compd.*, 2005, **404**, 706–711.
35 G. Barkhordarian, T. Klassen and R. Bormann, *J. Phys. Chem. B*, 2006, **110**, 11020–11024.
36 H. E. Kissinger, *Anal. Chem.*, 1957, **29**, 1702–1706.
37 M. Au, A. Jurgensen and K. Zeigler, *J. Phys. Chem. B*, 2006, **110**, 26482–26487.
38 Y. H. Guo, X. B. Yu, L. Gao, G. L. Xia, Z. P. Guo and H. K. Liu, *Energy Environ. Sci.*, 2010, **3**, 465–470.
39 J. Urgnani, F. J. Torres, M. Palumbo and M. Baricco, *Int. J. Hydrogen Energy*, 2008, **33**, 3111–3115.
40 L. C. Yin, P. Wang, Z. Z. Fang and H. M. Cheng, *Chem. Phys. Lett.*, 2008, **450**, 318–321.
41 E. H. Majzoub, J. L. Herberg, R. Stumpf, S. Spangler and R. S. Maxwell, *J. Alloys Compd.*, 2005, **394**, 265–270.
42 D. Syamala, V. Rajendran, R. K. Natarajan and S. M. Babu, *Cryst. Growth Des.*, 2007, **7**, 1695–1698.
43 R. Gosalawit-Utke, J. M. Bellosta von Colbe, M. Dornheim, T. R. Jensen, Y. Cerenius, C. B. Minella, M. Peschke and R. Bormann, *J. Phys. Chem. C*, 2010, **114**, 10291–10296.
44 T. T. Xu, J.-G. Zheng, N. Wu, A. W. Nicholls, J. R. Roth, D. A. Dikin and R. S. Ruoff, *Nano Lett.*, 2004, **4**, 963–968.
45 E. Muetterties, R. Merriefield, H. Miller, W. Knoth and R. Downing, *J. Am. Chem. Soc.*, 1962, **84**, 2506–2508.
46 R. Caputo, S. Garroni, D. Olid, F. Teixidor, S. Surinach and M. D. Baro, *Phys. Chem. Chem. Phys.*, 2010, **12**, 15093–15100.
47 S. Patil, G. Adhikary, G. Balakrishnan and K. Maiti, *Solid State Commun.*, 2011, **151**, 326–328.
48 G. Mavel, J. Escard, P. Costa and J. Castaing, *Surf. Sci.*, 1973, **35**, 109–116.
49 E. Deprez, M. A. Muñoz-Márquez, M. A. Roldán, C. Prestipino, F. J. Palomares, C. B. Minella, U. Bosenberg, M. Dornheim, R. Bormann and A. Fernández, *J. Phys. Chem. C*, 2010, **114**, 3309–3317.
50 E. Deprez, M. A. Muñoz-Márquez, M. C. Jimenez de Haro, F. J. Palomares, F. Soria, M. Dornheim, R. Bormann and A. Fernández, *J. Appl. Phys.*, 2011, **109**, 1–10.
51 U. Bosenberg, S. Doppiu, L. Mosegaard, G. Barkhordarian, N. Eigen, A. Borgschulte, T. R. Jensen, Y. Cerenius, O. Gutfleisch, T. Klassen, M. Dornheim and R. Bormann, *Acta Mater.*, 2007, **55**, 3951–3958.
52 U. Bosenberg, J. W. Kim, D. Gosslar, N. Eigen, T. R. Jensen, J. M. Bellosta von Colbe, Y. Zhou, M. Dahms, D. H. Kim, R. Gunther, Y. W. Cho, K. H. Oh, T. Klassen, R. Bormann and M. Dornheim, *Acta Mater.*, 2010, **58**, 3381–3389.
53 D. Pottmaier, C. Pistidda, E. Groppo, S. Bordiga, G. Spoto, M. Dornheim and M. Baricco, *Int. J. Hydrogen Energy*, 2011, **36**, 7891–7896.
54 J. F. Mao, X. B. Yu, Z. P. Guo, H. K. Liu, Z. Wu and J. Ni, *J. Alloys Compd.*, 2009, **479**, 619–623.
55 J. F. Mao, X. B. Yu, Z. P. Guo, C. K. Poh, H. K. Liu, Z. Wu and J. Ni, *J. Phys. Chem. C*, 2009, **113**, 10813–10818.
56 J. F. Mao, Z. P. Guo, H. Y. Leng, Z. Wu, Y. H. Guo, X. B. Yu and H. K. Liu, *J. Phys. Chem. C*, 2010, **114**, 11643–11649.
57 C. Bonatto Minella, S. Garroni, C. Pistidda, R. Gosalawit-Utke, G. Barkhordarian, C. Rongeat, I. Lindemann, O. Gutfleisch, T. R. Jensen, Y. Cerenius, J. Christensen, M. D. Baró, R. Bormann, T. Klassen and M. Dornheim, *J. Phys. Chem. C*, 2011, **115**, 2497–2504.

58 P. J. Wang, L. P. Ma, Z. Z. Fang, X. D. Kang and P. Wang, *Energy Environ. Sci.*, 2009, **2**, 120–123.
59 R. Gosalawit-Utke, K. Suarez, J. M. Bellosta von Colbe, U. Bosenberg, T. R. Jensen, Y. Cerenius, C. B. Minella, C. Pistidda, G. Barkhordarian, M. Schulze, T. Klassen, R. Bormann and M. Dornheim, *J. Phys. Chem. C*, 2011, **115**, 3762–3768.
60 R. E. Thoma, *Inorg. Chem.*, 1962, **1**, 220–226.
61 S. V. Meschel and O. J. Kleppa, *J. Chim. Phys. Phys.-Chim. Biol.*, 1993, **90**, 349–354.
62 P. Wang, X. D. Kang and H. M. Cheng, *J. Phys. Chem. B*, 2005, **109**, 20131–20136.
63 A. Roine, *Outokumpu HSC Chemistry for Windows: Chemical Reaction and Equilibrium Software with Extensive Thermodynamical Database and Flowsheet Simulation, Version 6.0*, 06120-ORC-T, Outokumpu Research Oy, Finland, 2006.
64 J. H. Shim, J. H. Lim, S. U. Rather, Y. S. Lee, D. Reed, Y. H. Kim, D. Book and Y. W. Cho, *J. Phys. Chem. Lett.*, 2010, **1**, 59–63.